

Fast and efficient demultiplexing of single photons from a quantum dot with resonantly enhanced electro-optic modulators

Julian Münzberg,^{1, a)} Franz Draxl,¹ Saimon Filipe Covre da Silva,² Yusuf Karli,¹ Santanu Manna,² Armando Rastelli,² Gregor Weihs,¹ and Robert Keil¹

¹⁾*Institut für Experimentalphysik, Universität Innsbruck, Technikerstr. 25, 6020 Innsbruck, Austria*

²⁾*Institute of Semiconductor and Solid State Physics, Johannes Kepler University Linz, 4040 Linz, Austria*

(Dated: 17 March 2022)

We report on a multi-photon source based on active demultiplexing of single photons emitted from a resonantly excited GaAs quantum dot. Active temporal-to-spatial mode demultiplexing is implemented via resonantly enhanced free-space electro-optic modulators, making it possible to route individual photons at high switching rates of 38 MHz. We demonstrate routing into four spatial modes with a high end-to-end efficiency of $\approx 79\%$ and measure a four-photon coincidence rate of 0.17 Hz mostly limited by the single-photon source brightness and not by the efficiency of the demultiplexer itself. We use the demultiplexer to characterize the pairwise indistinguishability of consecutively emitted photons from the quantum dot with variable delay time.

I. INTRODUCTION

The interference of multiple non-interacting, indistinguishable particles is the driving mechanism behind the rich dynamics of multi-photon quantum optics^{1–5} and sets the stage for advanced quantum information protocols, such as boson sampling,^{6–10} quantum simulation,^{11,12} and quantum networks.¹³ The required multi-photon states are typically generated by spontaneous parametric down conversion (SPDC) sources.^{14,15} Via advanced source engineering^{16,17} or tight spectral filtering,¹⁸ these sources produce photons with almost perfect indistinguishability and degree of entanglement.¹⁹ Nevertheless, due to the probabilistic nature of the SPDC process there is an inherent and unavoidable trade-off between the source brightness and an undesired background from higher-order emissions.

This severe limitation can be avoided by using true single-photon emitters, such as epitaxial semiconductor quantum dots (QDs) which, by virtue of the deterministic nature of the emission process, offer an alternative route towards on-demand generation of multi-photon states with precisely defined photon number.²⁰ By collecting the emission of n remote QDs pumped by the same excitation laser, an n -photon source can, in principle, be constructed. However, it has proven difficult to generate indistinguishable photons from separate QDs due to variations in the QDs' structural properties and noise in their solid-state environment. In order to obtain a source of multiple indistinguishable photons from remote QDs, the emission wavelengths of the emitted photons, as well as the spectral and temporal overlap of the wavepackets need to be exactly matched. Moreover, the noise in the solid-state environment needs to be eliminated. Nevertheless, just recently, two-photon interference (TPI) between photons from two remote QDs with a visibility of

93% was demonstrated.²¹ Despite this result, it remains difficult to scale this method to a larger number of photons due to the required experimental overhead. Upscaling demands either expensive equipment (a cryostat per QD single-photon source) or sophisticated optics to couple the emission of multiple QDs from a single sample into separate optical fibers in addition to electric control of individual QDs.

Alternatively, it is also possible to implement a multi-photon source by temporal-to-spatial mode demultiplexing, where m consecutively emitted photons from a single QD are routed into m spatial modes. Probabilistic demultiplexing with passive beamsplitters only constitutes a non-scalable approach as the detected m -photon rate scales with $(1/m)^m$.⁸ On the other hand, active demultiplexing, our method of choice, is a scalable approach. Here, a photon in a particular temporal mode is actively and deterministically routed into a particular spatial mode with e.g. electro-optic modulators (EOMs) and polarizing beamsplitters. Experimentally, active temporal-to-spatial demultiplexing was implemented in an integrated lithium niobate waveguide with four photons (with a fast switching rate of 40 MHz but low overall efficiency, due to waveguide-induced losses),²² in low-loss free-space setups via broadband EOMs (slow switching at ≈ 1 MHz) and polarizing beamsplitters with four²³ and 20 photons⁹ (of which 14 photons were detected), as well as with an acousto-optic modulator (slow switching at ≈ 1.4 MHz).²⁴

We use in this work resonantly enhanced EOMs that require much lower half-wave voltages compared to their broadband counterpart and allow for much faster switching rates. Therefore, our implementation sets itself apart from the previous ones by demonstrating high switching rates (switching of individual photons at 38 MHz) and high efficiency at the same time. A high switching rate allows us to route photons one-by-one instead of in bursts which is advantageous in terms of indistinguishability and detector dead time (see Sec. V for more

^{a)}Electronic mail: julian.muenzberg@uibk.ac.at

details).

As a single-photon source, we use GaAs QDs grown by droplet etching epitaxy,²⁵ which emit in the range of 780-805 nm wavelength. They have excellent emission properties, among them a high single-photon purity,²⁶ near zero fine structure splitting,²⁷ and fast radiative decay rates, which makes these QDs appealing single-photon and entangled photon pair sources.^{25,28}

In this work, we implement active temporal-to-spatial mode demultiplexing of photons from a GaAs QD single-photon source into four spatial modes. Pulsed resonant excitation of the QD allows us to generate a train of single photons in well defined temporal modes (ideally a single photon per excitation laser pulse). Subsequently, we actively route the train of single photons into four spatial modes with resonantly enhanced EOMs and polarizing beam splitters (PBSs). Compared to other excitation schemes, resonant excitation yields the highest photon indistinguishability between consecutively emitted photons,^{29,30} which is beneficial for multi-photon interference experiments.

This work is structured as follows. In Sec. II, we describe the experimental setup for single-photon creation and routing. We present the performance of our QD single-photon source, as well as the demultiplexer in Sec. III, and, as a proof of concept of our device, measure the indistinguishability of the QD emission at various time delays in Sec. IV. Finally, we conclude in Sec. V.

II. DEMULTIPLEXING SINGLE PHOTONS FROM A QUANTUM DOT

Figure 1 shows the experimental setup, which consists of three parts: Single photon generation in the QD setup via resonance fluorescence (red box), active temporal-to-spatial mode demultiplexing in the routing setup (green box), and, lastly, single-photon detection and coincidence counting (yellow box). Our GaAs QD sample is grown with the local droplet etching technique by molecular beam epitaxy. The QD layer is located in the center of a planar lambda cavity to enhance the extraction efficiency from the high refractive index material (for more details on the sample structure see Sec. S1 in the [supplementary material](#)). From a finite difference time domain simulation of the structure, we retrieve an extraction efficiency of $\eta_{\text{extr}} \approx 0.12$ (collected into an NA of 0.77) and from a mode overlap calculation of the QD emission with a single-mode fiber we obtain as fiber-coupling efficiency $\eta_{\text{fibercoup}} \approx 0.60$.

The QD sample is situated on a three-axis piezoelectric stage inside a closed-cycle cryostat with a base temperature of $\approx 8\text{K}$. We excite the QD with a pulsed Ti:Sapphire laser (Coherent Mira 900) with a repetition rate $RR = 76.2\text{MHz}$ and a pulse duration of $\approx 6\text{ps}$ (after spectral filtering in a $4f$ pulse shaper). The excitation laser is focused onto the QD with a cold aspheric lens (NA = 0.77) inside the cryostat so that a stable coupling

efficiency of the QD emission to the single-mode fiber is maintained over days.

For laser rejection under resonant excitation, we rely on the so-called cross-polarized excitation/collection configuration.³¹ In our setup, the excitation laser passes a nanoparticle linear film polarizer (extinction ratio $> 10^5 : 1$) in order to set the polarization to vertical before reflecting off a PBS and propagating towards the QD sample. Ideally, any back-reflected or back-scattered laser light is still vertically polarized and therefore blocked from transmitting into the collection path by the PBS (extinction ratio $> 10^3 : 1$) and an additional Glan-Taylor polarizer (extinction ratio $> 10^5 : 1$). Thus, only the horizontally polarized emission from the QD is transmitted and coupled into a polarization-maintaining single-mode fiber. We use a quarter-wave plate (QWP) to compensate for small amounts of birefringence in the sample path which can cause a deviation from vertical polarization of any reflected laser light. A half-wave plate (HWP) is used to set the excitation polarization of the QD, which acts as a full-wave plate for the reflected laser, since it passes the waveplate twice. The two waveplates and the nanoparticle linear film polarizer are mounted on high-precision piezo-driven rotation stages with a minimal incremental motion of $5\mu\text{rad}$, which is important to precisely optimize the laser rejection.

The output of the QD setup is connected to the input of the routing setup. Here, the light is coupled out of the fiber, passes through a QWP (see below for its role) and an EOM (QUBIG AM7R3-NIR-39). We apply a sinusoidal voltage to the EOM with a frequency equal to half the repetition rate of the pump laser $f_{\text{EOM}} = RR/2 = 38.1\text{MHz}$ and an amplitude equal to half the half-wave voltage $V_{\pi}/2$ of the EOM. In resonantly enhanced EOMs, the electro-optic crystal is embedded in a high- Q resonant LC circuit which boosts the RF voltage across the crystal (the capacitor in the LC circuit) at the resonance frequency. Therefore, significantly less input voltage ($V_{\pi} \approx 10\text{V}$) is required compared to broadband EOMs ($V_{\pi} > 1\text{kV}$). The applied sinusoidal voltage is phase locked to the pump laser via a reference clock input and a phase-locked loop (PLL). The QWP oriented at 45° transforms the initially linear polarization to circular polarization, which is equivalent to biasing the EOM at $V_{\pi}/2$. Due to the biasing, a full modulation from vertical to horizontal polarization is achieved. If the phase of the applied sinusoidal voltage (with respect to the reference clock) is set such that a photon passes through the EOM at the maximum or minimum of the sinusoidal modulation, then every second photon will be switched from vertical to horizontal polarization. Subsequently, the photons are routed according to their polarization with a PBS. Then, in the absence of losses, in transmission (reflection) every second time bin (duration $\Delta t = 13.1\text{ns} = RR^{-1}$) would be occupied by a horizontally (vertically) polarized photon, respectively, and all other time bins would be empty. The non-linear transfer function (Malus' Law) of the EOM-PBS system causes a

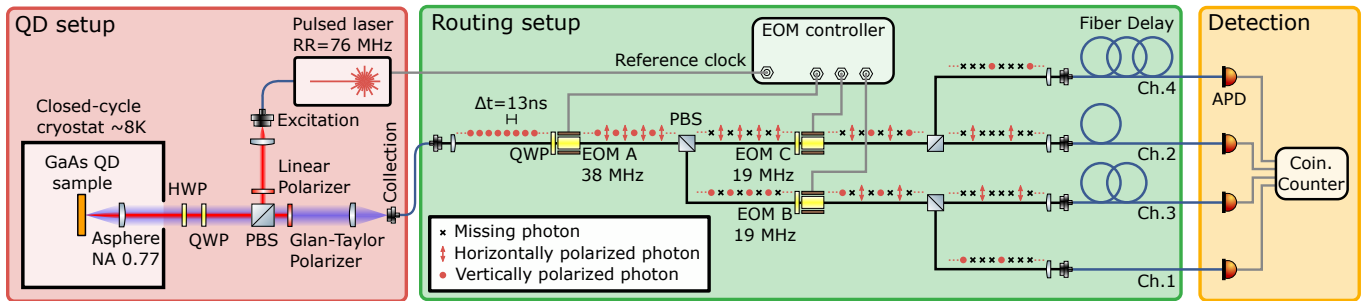


FIG. 1. A schematic illustration of the experiment with the QD setup (red box), the routing setup (green box), and the detection setup (yellow box). A detailed description of the setup is found in Section II.

flattening of the minima and maxima of the transmission (reflection) function in time, such that the adjustment of the relative phase to the pump laser and the half-wave voltage is uncritical (see Sec. S2 in the [supplementary material](#) for more details).

In the second stage of the routing setup, we use two beam lines each with a QWP, an EOM (QUBIG AM7R3-NIR-19) operated at a quarter of the pump laser repetition rate $f_{\text{EOMB}} = f_{\text{EOMC}} = RR/4 = 19.05$ MHz, and a PBS to route four photons in four consecutive time bins into four spatial modes labelled Ch. 1 to 4. Furthermore, we compensate the temporal delay between the photons by using different fiber lengths of 2 m, 4.7 m, 7.4 m, and 10.1 m for Ch. 1 to 4, respectively. In order to make the photons also indistinguishable in their polarization degree of freedom, the fiber couplers in Ch. 1 and 4 are rotated by 90° with respect to the fiber couplers in Ch. 2 and 3, such that the light is always coupled into the fast axis of the polarization-maintaining single-mode fiber.

In order to measure the four-photon coincidence rate of our multi-photon source, we attach each output channel to an avalanche photodiode (APD) and use a coincidence counter to measure the four-photon coincidence rate.

III. PERFORMANCE OF THE MULTI-PHOTON SOURCE

First, we characterize the performance of our QD single-photon source in terms of brightness and single-photon purity. By turning off all EOMs and removing the QWPs from the routing setup, ideally all light is routed towards Ch. 1 (compare Fig. 1), which can be connected to a spectrometer or an APD depending on the type of measurement. In this configuration of the routing setup, the routing efficiency into Ch. 1 is $\eta_{\text{Ch1}} = 0.91(4)$ (obtained from a separate measurement with laser light).

Figure 2 shows the recorded data for the one QD which is used as the single-photon source throughout this work. In Fig. 2(a), the spectrum under above bandgap excitation with 532 nm laser light is shown on a logarithmic scale. The neutral exciton transition corresponds to a wavelength of 798.66 nm. Figure 2(c) shows the spectrum under pulsed resonant s-shell excitation of the ex-

citon. In this case, we tune the center wavelength of the pump laser exactly in resonance with the exciton transition, such that we only observe fluorescence from the pronounced zero-phonon line of the exciton, as well as a very weak phonon sideband (visible as pedestal of the main peak). Next, we measure the QD fluorescence signal as a function of the excitation laser power. The signal is monitored with an APD (detection efficiency $\eta_{\text{det}} \approx 68(5)\%$) without any spectral filtering of the signal. The result is plotted in Fig. 2(b), which shows a clear modulation of the signal indicative of Rabi oscillations up to a pulse area of $\approx 5\pi$ with a maximum detected count rate of 425(4) kHz at a pulse area of π . By fitting the data (see Sec. S3 in the [supplementary material](#)) we retrieve a population probability η_{pop} of the neutral exciton of 90.9(5)%. Above a pulse area of 3π , the signal deviates from the damped Rabi-oscillation-like behavior most probably due to laser leakage and off-resonant excitation of additional emission lines. The latter is confirmed by recording the spectrum for excitation powers $> 3\pi$. The spectrum shown in Fig. 2(c) is recorded at π -pulse excitation.

Also at π -pulse excitation, we measure the single-photon purity in a Hanbury Brown and Twiss (HBT) measurement. We perform the measurement by again inserting the QWP before EOM A such that half the light is probabilistically guided towards output Ch. 2 and half the light towards output Ch. 1, which are each connected to an APD. All EOMs are still turned off. We record the correlation histogram shown in Fig. 2(d) and retrieve a second-order correlation function at zero time delay of $g^{(2)}(0) = 0.016(1)$ by taking the ratio of the integrated counts of the center peak to the average integrated counts of the side peaks. The measured single-photon purity of our source is limited by the residual pump laser and re-excitation processes. Furthermore, we measure the lifetime of the neutral exciton under pulsed resonant excitation. We obtain a lifetime of 167(8) ps and a fine structure splitting of 9.7(2) μeV (see Sec. S4 in the [supplementary material](#)).

From the detected count rate R_{det} at π -pulse excitation, we can calculate the fiber-coupled efficiency of our QD single-photon source η_{QD} , which includes all loss contributions from the source up to the routing setup.

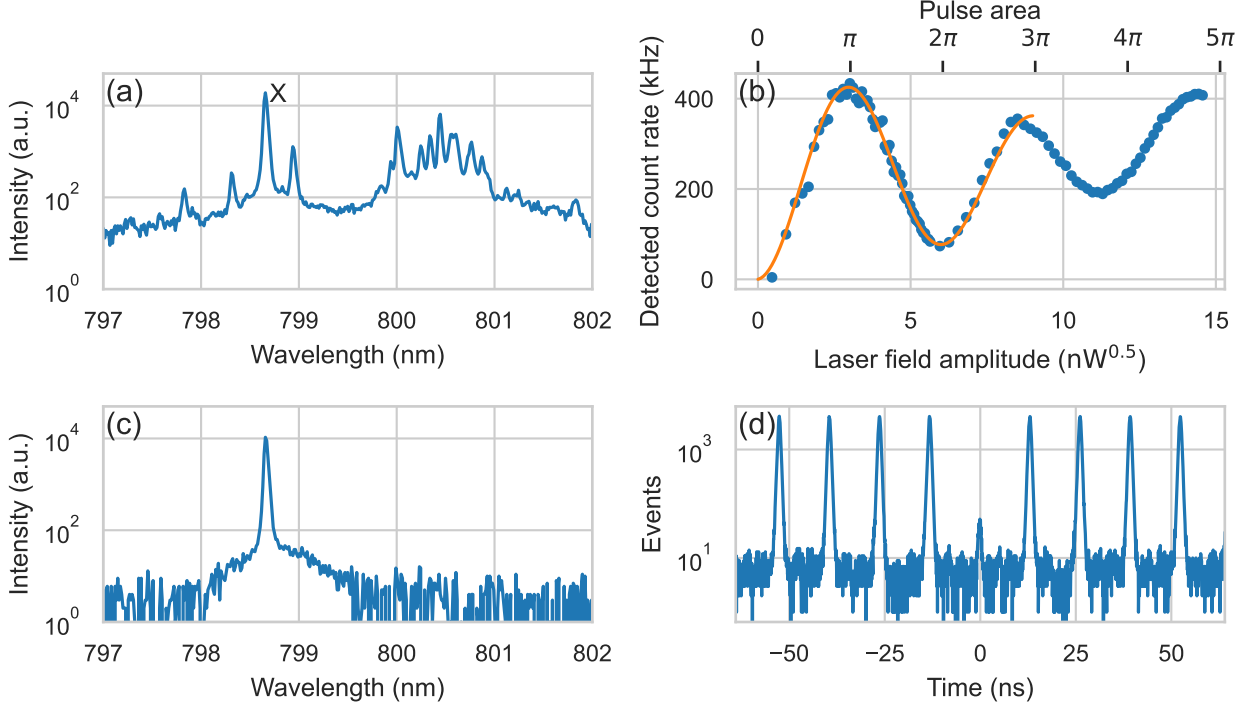


FIG. 2. Characterization of the QD emission. (a) Background-subtracted spectrum of the QD under above bandgap excitation with laser light at 532 nm. The neutral exciton (X) emission wavelength is 798.66 nm. (b) Power-dependent Rabi oscillations of the neutral exciton up to a pulse area of approx. 5π . The detected single-photon count rate reaches a maximum of $\approx 425(4)$ kHz at a π -pulse power of 9 nW (measured in front of the cryostat window, focused laser beam diameter $\approx 1.5 \mu\text{m}$). For π -pulse excitation, we extract an excited state population probability of 90.9(5)% from the fit (orange line). (c) Background-subtracted spectrum of the QD under pulsed resonant s -shell excitation with a π -pulse. (d) Second-order intensity correlation histogram under pulsed resonant excitation with $g^{(2)}(0) = 0.016(1)$.

These are the finite population probability η_{pop} , blinking of the QD with an on-time-fraction of η_{blinking} ,³² the finite extraction efficiency η_{extr} from the sample, losses in the optical elements of the QD setup with η_{optics} , and the fiber-coupling efficiency of the QD mode to the fiber mode $\eta_{\text{fibercoup}}$. The estimated fiber-coupled source efficiency is

$$\eta_{\text{QD}} = \frac{R_{\text{det}}}{RR} \frac{1}{\eta_{\text{Ch1}}\eta_{\text{det}}} = 0.90(9)\%. \quad (1)$$

The fiber-coupled source efficiency can also be estimated from the above mentioned loss contributions (see Sec. S5 in the [supplementary material](#)).

Next, we characterize the efficiency of the routing setup with classical laser pulses. We connect the pump laser, which is otherwise used to excite the QD, directly to the input of the routing setup. The continuous-wave-equivalent power of the laser is $\approx 100 \mu\text{W}$ (measured free-space after the input coupler of the routing setup). Then, we measure the fiber-coupled power in all four output channels with a powermeter (Thorlabs PM110D and photodiode sensor S121C) and calculate the channel efficiency from the ratio of measured power divided by laser input power. We obtain an efficiency of 22.5(10)%,

19.9(8)%, 21.4(9)%, and 19.9(8)% for output Ch. 1 to 4, respectively, resulting in a combined efficiency of all channels of $\eta_{\text{routing}} = 84(3)\%$. This does not yet include a reduction in the efficiency due to erroneous switching as a consequence of the finite extinction ratio of the EOMs, since we measure the power in a time-integrated fashion. We also measure the fiber-coupling efficiency of each output channel, obtained as the ratio of power measured in the fiber to power measured free-space in front of the fiber coupler. Here, we obtain values of 95(4)%, 89(4)%, 89(4)%, and 87(4)% for Ch. 1 through 4, respectively. We suspect that the variation in coupling efficiency is due to variations in the fiber coupler lens quality and in the wavefront error induced by the optical elements in the setup e.g. the PBSs.

In the next step, we characterize the switching efficiency of the routing setup η_{sw} given by the ratio of correctly routed events to the total number of events. The results shown in Fig. 3 are obtained with light from the QD single-photon source. We perform a start-stop-measurement, where the internal photodiode of the pump laser serves as a start signal (the clock is started only every fourth pulse) and the detection of a photon in either of the four output channels stops the clock. The

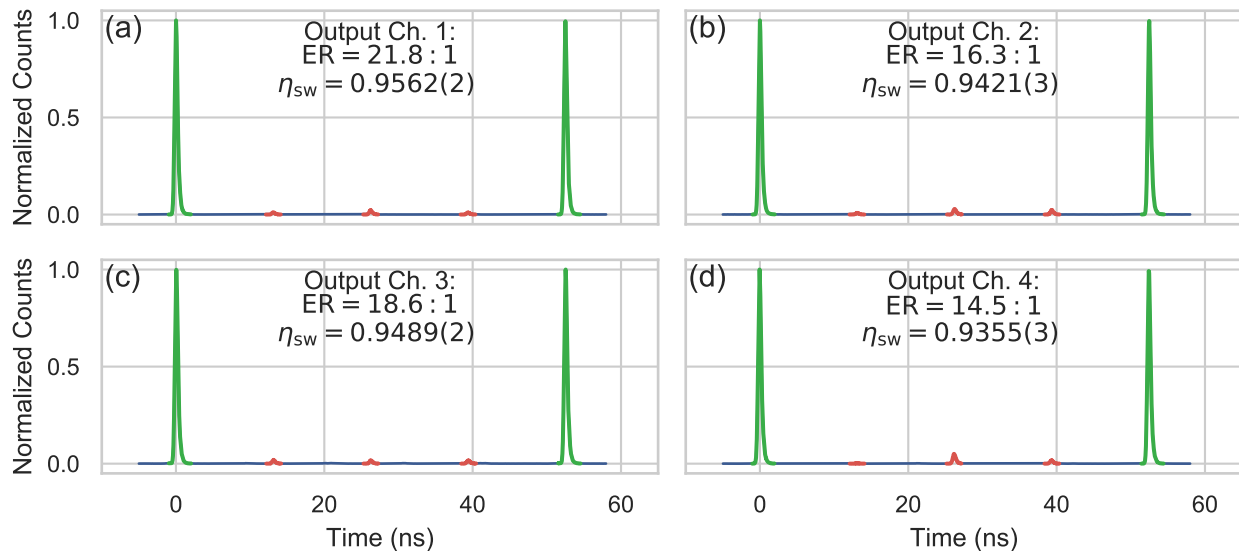


FIG. 3. Normalized histogram of accumulated time differences between the pump laser and the four output channels of the demultiplexer. Every fourth pump pulse starts the clock and the detection of a photon in an output channel stops the clock. The extinction ratio of the four output channels is calculated from the ratio of integrated counts of the main peak (green) to the sum of integrated counts of the side peaks (red). The uncertainty of the switching efficiency is calculated from the Poissonian counting statistics.

time differences are then accumulated into a histogram. Ideally, one should only observe peaks in the histogram separated by $4\Delta t = 52.5$ ns. These peaks are indicated in green color in Fig. 3. In the experiment, we observe additional peaks marked in red that correspond to incorrectly routed events. There are three different combinations of incorrect routing which correspond to the three side peaks in Fig. 3. Such an incorrectly routed event could e.g., be produced in the following way: Suppose that the photon in the second time bin in Fig. 1 is incorrectly routed in transmission through the first PBS towards EOM C. It could therefore be routed towards channel 2 or 4 and produce an event corresponding to a time difference of 13.1 ns in Fig. 3(b) or 39.4 ns in Fig. 3(d), respectively. There are also other erroneous routing events, which, combined, lead to the red side peaks in Fig. 3. The peak heights of the three side peaks are marginally different due to a slight variation of the individual extinction ratios (ERs) of the EOMs, a different ER of the PBS in transmission and reflection, and the exact alignment conditions. For each output channel, we calculate the channel ER as the ratio of the average integrated counts of the main peaks Σ_{main} to the sum of integrated counts of the three side peaks Σ_{side} , as well as the switching efficiency $\eta_{\text{sw}} = \Sigma_{\text{main}} / (\Sigma_{\text{main}} + \Sigma_{\text{side}})$. The results are summarized in Fig. 3 from which we calculate an average switching efficiency across all channels of $\eta_{\text{sw}} = 0.946(8)$, where the uncertainty is given by the standard deviation of the four single-channel switching efficiencies. An advantage of our specific setup design is that an incorrectly routed photon will never end up in the

same time bin as a correctly routed photon. A fourfold coincidence is therefore either produced by four correctly routed photons or four incorrectly routed photons, with the former being about 10^6 times more likely.

In an active m -mode demultiplexer, the detected n -fold coincidence rate of n distinct channels clicking simultaneously ($n \leq m$) is given by (adapted from Ref. 22—we additionally take into account blinking of the QD and differentiate between m and n)

$$R(n) = \frac{RR}{m} \eta_{\text{blinking}} \left(\frac{\eta_{\text{QD}} \eta_{\text{routing}} \eta_{\text{det}}}{\eta_{\text{blinking}}} \right)^n \times \left[\eta_{\text{sw}}^n + (m-1) \left(\frac{1-\eta_{\text{sw}}}{m-1} \right)^n \right]. \quad (2)$$

The first and the second summand in the square bracket term corresponds to a coincidence due to n correctly routed photons and the $(m-1)$ possible cases of n incorrectly routed photons, respectively. A passive demultiplexer would correspond to $\eta_{\text{sw}} = 0.25$ such that the square bracket term simplifies to m/m^n . Blinking of the QD—that is an *on-off*-type behavior of its photoluminescence intensity—manifests itself in a different scaling compared to the other efficiencies in Eq. (2). If the blinking timescale is long compared to the switching cycle time m/RR , then the detected coincidence rate scales linearly with the on-time-fraction η_{blinking} and not with η_{blinking}^n since on average the QD is either *on* for the complete switching cycle or *off*. This is different for the other efficiencies, since they are completely uncorrelated in time. For the investigated QD, we measure an on-time-fraction

of $\eta_{\text{blinking}} = 0.36$ and a blinking timescale in the order of milliseconds, much longer than the switching cycle time 52.5 ns (see Sec. S6 in the [supplementary material](#) for a comparison of the blinking behavior without and with additional above bandgap illumination of the sample).

For our four-mode demultiplexer, the measured and calculated n -fold coincidence rates are summarized in Tab. I. The measured mean n -fold rate agrees well with the expected n -fold rate, which is calculated according to Eq. (2) and the measured efficiencies of the setup. We measure a four-photon coincidence rate of 0.17(1) Hz over a measurement time of ≈ 15 h, detecting in total 8.7×10^3 fourfold coincidence events. We noticed that $g^{(2)}(0)$ increased from initially $g^{(2)}(0) = 0.016$ before the measurement to $g^{(2)}(0) = 0.116$ after the measurement, most probably due to a degradation in the cross-polarized laser suppression. While this slightly increased the single count rates over the course of the measurement ($\sim 8\%$), it had almost no influence on the detected four-photon coincidence rate (see Sec. S7 in the [supplementary material](#)). The device can also be used as a three-photon source by only connecting e.g. output Ch. 1, 3, and 4, where we obtain a three-photon rate of 14.6 Hz.

IV. PHOTON INDISTINGUISHABILITY AT VARYING EXCITATION PULSE SEPARATIONS

The routing setup can be used to characterize the indistinguishability of consecutively emitted photons from the QD via Hong-Ou-Mandel (HOM)-type TPI.^{1,20,33} We perform TPI at pump pulse separations of 13.1, 26.2, and 39.4 ns, which is implemented by connecting output Ch. 1 to one input and output Ch. 2, 3, or 4 to the other input of a polarization-maintaining 50/50 fiber beamsplitter. The outputs of the beamsplitter are attached to APDs. We obtain the correlation histograms shown in Fig. 4 for a co-polarized and a cross-polarized input to the beamsplitter. Cross-polarized input is achieved by placing a HWP oriented at 45° in front of the fiber coupler of Ch. 1. Before the measurement, we adjust the temporal overlap of the photons at the beamsplitter with the procedure described in Sec. S8 in the [supplementary material](#). We calculate the raw HOM visibility from

$$V_{\text{raw}} = 1 - \frac{C_{\parallel}}{C_{\perp}}, \quad (3)$$

where C_{\parallel} and C_{\perp} are the normalized coincidence counts integrated over the central peak for the co-polarized and cross-polarized configuration, respectively. The three small peaks in between the central peak and the main uncorrelated peaks (uncorrelated peak e.g. at 52.5 ns) correspond to the cross-correlation between a correctly routed photon in one channel and an incorrectly routed photon in another channel or vice versa. Correcting for an imperfect splitting ratio of the beamsplitter and a non-zero

$g^{(2)}(0)$, the indistinguishability is given by³³

$$V = \frac{V_{\text{raw}} + g^{(2)}(0)}{1 - g^{(2)}(0)} \frac{R^2 + T^2}{2RT}, \quad (4)$$

with the beamsplitter intensity reflectivity (transmissivity) $R = 0.514(7)$ ($T = 1 - R$), as well as $g^{(2)}(0) = 0.016(1)$. We obtain corrected indistinguishabilities of $V_{13.1 \text{ ns}} = 0.803(5)$, $V_{26.2 \text{ ns}} = 0.826(4)$, and $V_{39.4 \text{ ns}} = 0.774(4)$.

The photon indistinguishability is approximately constant for the three investigated excitation pulse separations. The obtained value for 39.4 ns is slightly smaller than for the two shorter temporal delays, but this might be caused by uncertainties in the measurement e.g. imperfect perpendicular polarization in the cross-polarized measurement. We expect that this is the case, since the area of the center peak for the cross-polarized measurement in Fig. 4(c) is smaller than half the area of the uncorrelated peaks. This might underestimate V_{raw} in Eq. (3). If we instead calculate $V'_{\text{raw}} = 1 - 2A$ where A is the ratio of the area of the center peak to the average area of the uncorrelated peaks, then we obtain a value of $V'_{39.4 \text{ ns}} = 0.795$ very close to the values obtained for the other two temporal delays.

A degradation in the indistinguishability for larger excitation pulse separation is expected due to charge fluctuations in the vicinity of the QD. Charge-noise causes spectral diffusion and an inhomogeneous broadening of the QD transition.³⁴ It has been shown that a degradation is already present at short timescales for the GaAs QDs studied here and excited via two-photon excitation ($V = 0.62$ at 2 ns and $V = 0.43$ at 12.5 ns pulse separation),³⁵ as well as LO-phonon excitation ($V = 0.92$ at 4 ns and $V = 0.78$ at 12 ns),²⁹ and in InGaAs QDs excited quasi-resonantly ($V = 0.94$ at 2 ns and $V = 0.53$ at 12.5 ns).³⁴ The above findings are confirmed by photon-correlation Fourier spectroscopy, which directly probes the timescale of spectral diffusion of the QD transition.³⁶ From these examples we conclude that charge-noise is the main cause of the imperfect indistinguishability observed in our measurement, given the large pulse separation times in our measurement. Furthermore it has been shown for InGaAs QDs, that for an even larger excitation pulse separations a plateau-like behavior is theoretically expected.³⁴ Our findings exhibiting a constant indistinguishability from 13.1 to 39.4 ns pulse separation indicate that such a plateau-like behavior can also be reached in the GaAs material system. Charge-noise can be strongly reduced by improved material quality and by embedding the QDs in charge-tunable devices as already demonstrated for InGaAs^{37,38} and GaAs²¹ QDs.

An additional mechanism possibly leading to a deterioration of photon indistinguishability is phonon-induced pure dephasing. In Ref. 34, the authors conclude that for InGaAs QDs a degradation in the photon indistinguishability is almost negligible for temperatures < 10 K, but has a significant effect at higher temperatures. In our

TABLE I. Measured and calculated count rates at the four output channels of the routing setup, as well as coincidence rates between all combinations of output channels.

							Mean ^a	Calculated ^b
Channel	1	2	3	4				
$R(1)$ (Hz)	104×10^3	91×10^3	103×10^3	96×10^3			$99(6) \times 10^3$	$98(13) \times 10^3$
Channel combinations	(1,2)	(1,3)	(1,4)	(2,3)	(2,4)	(3,4)		
$R(2)$ (Hz)	1093	1207	1134	1044	981	1085	$1.09(8) \times 10^3$	$1.3(3) \times 10^3$
Channel combinations	(1,2,3)	(1,2,4)	(1,3,4)	(2,3,4)				
$R(3)$ (Hz)	14.1	13.3	14.6	12.7			14.0(9)	17(7)
$R(4)$ (Hz)							0.17(1)	0.23(12)

^a *First row*: Mean count rate averaged over all channels. *Second and third row*: Mean n -fold coincidence rate averaged over all n -fold coincidence combinations. *Fourth row*: Fourfold coincidence rate of all four channels clicking simultaneously. For the fourfold coincidence rate, the measurement uncertainty is obtained from the Poissonian counting statistics.

^b Calculated according to Eq. (2) and taking into account the estimated efficiencies of the setup.

experiment we see that the TPI visibility keeps increasing when lowering the temperature from nominal 9 K to 8 K (see Sec. S9 in the [supplementary material](#)), indicating that the QD studied here may be particularly sensitive to phonon-induced pure dephasing. This finding is in line with the fact that the QD emits at a wavelength of almost 800 nm, which implies a large QD with small spacing among confined levels and consequently enhanced zero-phonon-line broadening due to virtual transitions to excited states.³⁹

The indistinguishability can potentially be improved by narrow-band spectral filtering which suppresses the phonon-sidebands at the cost of overall efficiency. Similarly, this can be realized by embedding the QD layer inside a narrow-band cavity.⁴⁰

V. COMPARISON AND CONCLUSION

We demonstrated active temporal-to-spatial demultiplexing by utilizing, for the first time, resonantly enhanced free-space EOMs. In Table II, we compare our work to other active temporal-to-spatial demultiplexing implementations. All other implementations so far have been performed with InGaAs QDs^{9,22,23} and the routing setup was either implemented with broadband free-space EOMs^{9,23}, integrated switches (with a low overall efficiency),²² or acousto-optic modulators. Compared to the broadband counterpart, resonantly enhanced EOMs require much lower half-wave voltages and therefore no bulky and expensive high-voltage amplifiers to drive the EOM. In addition, due to the lower half-wave voltage, these EOMs can be operated at much higher switching rates (in our case 38.1 MHz). This is beneficial, since the emission time separation between temporally overlapping photons after the demultiplexer is much shorter. In this work, the emission time separation is 13.1 to 39.4 ns compared to $\approx 1 \mu\text{s}$ in Ref. 9, 23, and 24. As dis-

cussed in Section IV, our demultiplexing implementation improves the indistinguishability of the photons by reducing the influence of charge-noise. For example in Ref. 24, the TPI visibility decreased from 92% at 12 ns to 76% at 960 ns emission time separation. In addition, a high switching rate is also advantageous in multi-photon interference experiments with current single-photon detection technology that relies on APDs and superconducting nanowire single-photon detectors (SNSPDs). These detectors have typical dead times in the order of tens of nanoseconds, which matches well with the switching cycle time of 52.5 ns of our demultiplexer. In contrast, in a demultiplexer with broadband EOMs operated at ≈ 1 MHz, the photons arrive in bunches of about 20 narrowly spaced photons and, therefore, the detection of a photon in the first time bin might render the detector unable to detect a photon in the subsequent time bins due to detector dead time. This might not be an issue for a lossy setup which makes it very unlikely that two consecutive time bins are both occupied with a photon, but becomes an important factor in the case of close to unity overall efficiency.

Our implementation of a demultiplexer results in an overall routing setup efficiency of $\eta_{\text{routing}}\eta_{\text{sw}} = 79(3)\%$ comparable to the implementations with broadband free-space EOMs^{9,23} and much better than the integrated implementation.²² We measure lower four-photon rates compared to Ref. 9 and 41 as a result of our much lower source brightness. With a source brightness of 26.1% as in Ref. 9, we predict a detected four-photon rate of $7(2) \times 10^3$ Hz with our demultiplexer. It is therefore crucial to increase the source brightness and reduce the overall losses in the setup as one can likewise infer from Eq. (2). The source brightness could be increased by embedding the GaAs QD into a micropillar or circular Bragg grating structure which should greatly improve the extraction efficiency.^{20,37,42,43}

The setup can be easily scaled up to a larger number

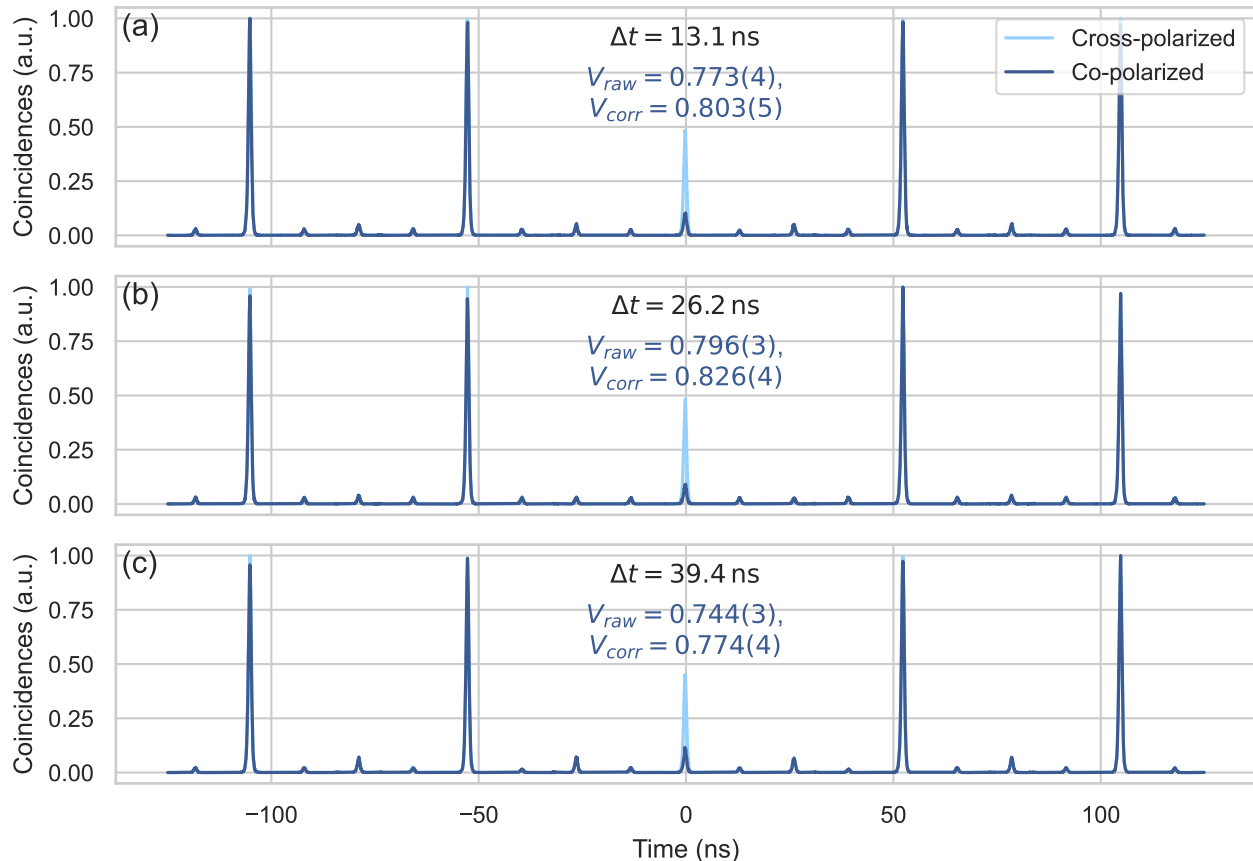


FIG. 4. Hong-Ou-Mandel interference measurements between different combinations of output channels from the routing setup. These combinations correspond to temporal delays between the interfering photons of (a) 13.1 ns, (b) 26.2 ns, and (c) 39.4 ns. The raw HOM visibility is calculated from the integrated counts of the central peak for the co- and cross-polarized case. V_{corr} is the HOM visibility corrected for an imperfect splitting ratio of the beamsplitter as well as a finite $g^{(2)}(0)$.

of 2^k (k being an integer) output channels e.g. 8 or 16. This is done by recursively adding an additional layer of four, eight or in general 2^{k-1} EOMs with a switching rate of $RR/8$, $RR/16$ or in general $RR/2^k$ to the previous setup. Additionally, due to the short decay time of the QD transition (typically 150-250 ps without resorting to Purcell enhancement), one could operate the single-photon source also at a higher pump rate of e.g. 152.4 MHz (obtainable by passive laser-pulse multiplexing), which would require an additional EOM operating at 76.2 MHz.⁴⁴ This would increase the obtainable multiphoton rate by a factor of two. Moreover, the demultiplexer can be used with any other single-photon source operated at a similar repetition rate and emission wavelength.

Active temporal-to-spatial mode demultiplexing of a QD single-photon source paves the way for truly deterministic multi-photon sources. This provides a feasible route towards multi-photon interference experiments with a large and precisely defined number of photons, which, so far, has been inaccessible with SPDC photon sources due to the probabilistic nature of their emission.

SUPPLEMENTARY MATERIAL

See the [supplementary material](#) for additional information on the sample structure, the EOM-PBS transmission function, the damped rabi oscillation model (fitting function in Fig. 2(b)), the lifetime of the QD emission, an overview of the QD setup efficiencies, an analysis of QD blinking, the timetrace of detected count rates, the interferometric path length adjustment procedure, and the temperature dependence of the TPI visibility.

ACKNOWLEDGMENTS

The authors acknowledge assistance from M. Aigner and fruitful discussions with M. Reindl, D. Huber, C. Schimpf and E. Vogt (QUBIG GmbH).

This work was financially supported by the Austrian Science Fund (FWF) via the projects P 30459 and I 4320 with D. Reiter, the Research Group FG5, the European Union's Horizon 2020 research and innovation pro-

TABLE II. Comparison of this work to other temporal-to-spatial demultiplexing implementations.

Reference	Photon source (excitation scheme)	Demultiplexer implementation	switching rate	η_{QD} $R_{\text{det}}^{\text{a}}$ R_{QD}^{b}	$\eta_{\text{routing}}\eta_{\text{sw}}$	measured $R(4)$
9	InGaAs QD in micropillar (resonant excitation)	Free-space, broadband EOMs	0.76 MHz	26.1% 16.3 MHz 19.9 MHz	84% ^c	$\approx 3000 \text{ Hz}^{\text{d}}$
23, 41	InGaAs QD in integrated waveguide (non-resonant excitation)	Free-space, broadband EOMs	0.95 MHz	2.8% 1.7 MHz 1.9 MHz	76.7% ($\eta_{\text{fiber}}\eta_{\text{sw}}\eta_{\text{m}}$) ^e	1.05 Hz
22	InGaAs QD in micropillar (quasi-resonant excitation)	Integrated switches in lithium niobate	40 MHz	$\approx 2.5\%$	23% (η_{DMT}) ^e	0.18 mHz (estimated)
24	InGaAs QD in micropillar (LA-phonon excitation)	Acousto-optic modulator	1.4 MHz	$\approx 9.5\%$	$\approx 65\%$	1.6 Hz ^d
This work	GaAs QD in planar cavity (resonant excitation)	Free-space, resonantly enhanced EOMs	38.1 MHz	0.90(9)% 0.425(4) MHz 0.69(7) MHz	79(3)%	0.17(1) Hz

^a Detected count rate of the QD single-photon source.

^b Count rate of the QD single-photon source corrected for detection efficiency.

^c It is not mentioned in Ref. 9 whether this value includes or excludes the switching efficiency η_{sw} of the setup.

^d After low loss linear optical network.

^e Variable names as given in the reference.

gram under Grant Agreements No. 899814 (Quoep) and No. 871130 (Ascent+), the Linz Institute of Technology (LIT), and the LIT Secure and Correct Systems Lab, supported by the State of Upper Austria.

AUTHOR DECLARATIONS

Conflict of Interest

The authors have no conflicts to disclose.

DATA AVAILABILITY STATEMENT

The data that support the findings of this study are openly available in Zenodo at <http://doi.org/10.5281/zenodo.6337697>.

REFERENCES

- ¹C. K. Hong, Z. Y. Ou, and L. Mandel, *Phys. Rev. Lett.* **59**, 2044 (1987).
- ²M. C. Tichy, *J. Phys. B At. Mol. Opt. Phys.* **47**, 103001 (2014).
- ³A. J. Menssen, A. E. Jones, B. J. Metcalf, M. C. Tichy, S. Barz, W. S. Kolthammer, and I. A. Walmsley, *Phys. Rev. Lett.* **118**, 153603 (2017).
- ⁴A. E. Jones, A. J. Menssen, H. M. Chrzanowski, T. A. W. Wolterink, V. S. Shchesnovich, and I. A. Walmsley, *Phys. Rev. Lett.* **125**, 123603 (2020).
- ⁵J. Münzberg, C. Dittel, M. Lebugle, A. Buchleitner, A. Szameit, G. Weihs, and R. Keil, *PRX Quantum* **2**, 020326 (2021).
- ⁶S. Aaronson and A. Arkhipov, in *Proceedings of the forty-third annual ACM symposium on Theory of computing* (2011) pp. 333–342.
- ⁷H. Wang, Y. He, Y.-H. Li, Z.-E. Su, B. Li, H.-L. Huang, X. Ding, M.-C. Chen, C. Liu, J. Qin, J.-P. Li, Y.-M. He, C. Schneider, M. Kamp, C.-Z. Peng, S. Höfling, C.-Y. Lu, and J.-W. Pan, *Nat. Photonics* **11**, 361 (2017).
- ⁸J. C. Loredó, M. A. Broome, P. Hilaire, O. Gazzano, I. Sagnes, A. Lemaitre, M. P. Almeida, P. Senellart, and A. G. White, *Phys. Rev. Lett.* **118**, 130503 (2017).
- ⁹H. Wang, J. Qin, X. Ding, M. C. Chen, S. Chen, X. You, Y. M. He, X. Jiang, L. You, Z. Wang, C. Schneider, J. J. Renema, S. Höfling, C. Y. Lu, and J. W. Pan, *Phys. Rev. Lett.* **123**, 250503 (2019).
- ¹⁰H.-S. Zhong, H. Wang, Y.-H. Deng, M.-C. Chen, L.-C. Peng, Y.-H. Luo, J. Qin, D. Wu, X. Ding, Y. Hu, P. Hu, X.-Y. Yang, W.-J. Zhang, H. Li, Y. Li, X. Jiang, L. Gan, G. Yang, L. You, Z. Wang, L. Li, N.-L. Liu, C.-Y. Lu, and J.-W. Pan, *Science* **370**, 1460 (2020).
- ¹¹A. Aspuru-Guzik and P. Walther, *Nat. Physics* **8**, 285 (2012).
- ¹²C. Sparrow, E. Martín-López, N. Maraviglia, A. Neville, C. Harrold, J. Carolan, Y. N. Joglekar, T. Hashimoto, N. Matsuda, J. L. O’Brien, D. P. Tew, and A. Laing, *Nature* **557**, 660 (2018).
- ¹³M. Pompili, S. L. Hermans, S. Baier, H. K. Beukers, P. C. Humphreys, R. N. Schouten, R. F. Vermeulen, M. J. Tiggelman, L. dos Santos Martins, B. Dirkse, S. Wehner, and R. Hanson, *Science* **372**, 259 (2021).
- ¹⁴Y. Shih, *Reports Prog. Phys.* **66**, 1009 (2003).
- ¹⁵A. Christ, A. Fedrizzi, H. Hübel, T. Jennewein, and C. Silberhorn, in *Single-Photon Generation and Detection*, Experimental

- Methods in the Physical Sciences, Vol. 45, edited by A. Migdall, S. V. Polyakov, J. Fan, and J. C. Bienfang (Academic Press, 2013) pp. 351–410.
- ¹⁶P. J. Mosley, J. S. Lundeen, B. J. Smith, P. Wasylczyk, A. B. U'Ren, C. Silberhorn, and I. A. Walmsley, *Phys. Rev. Lett.* **100**, 133601 (2008).
 - ¹⁷A. Pickston, F. Graffitti, P. Barrow, C. L. Morrison, J. Ho, A. M. Brańczyk, and A. Fedrizzi, *Opt. Express* **29**, 6991 (2021).
 - ¹⁸T. Scheidl, F. Tiefenbacher, R. Prevedel, F. Steinlechner, R. Ursin, and A. Zeilinger, *Phys. Rev. A* **89**, 042324 (2014).
 - ¹⁹M. Proietti, J. Ho, F. Grasselli, P. Barrow, M. Malik, and A. Fedrizzi, *Science Advances* **7**, eabe0395 (2021).
 - ²⁰P. Senellart, G. Solomon, and A. White, *Nat. Nanotechnol.* **12**, 1026 (2017).
 - ²¹L. Zhai, G. N. Nguyen, C. Spinnler, J. Ritzmann, M. C. Löbl, A. D. Wieck, A. Ludwig, A. Javadi, and R. J. Warburton, “Quantum interference of identical photons from remote quantum dots,” (2021), [arXiv:2106.03871 \[quant-ph\]](https://arxiv.org/abs/2106.03871).
 - ²²F. Lenzini, B. Haylock, J. C. Loredó, R. A. Abrahão, N. A. Zakaria, S. Kasture, I. Sagnes, A. Lemaitre, H.-P. Phan, D. V. Dao, P. Senellart, M. P. Almeida, A. G. White, and M. Lobino, *Laser Photonics Rev.* **11**, 1600297 (2017).
 - ²³T. Hummel, C. Ouellet-Plamondon, E. Ugur, I. Kulkova, T. Lund-Hansen, M. A. Broome, R. Uppu, and P. Lodahl, *Appl. Phys. Lett.* **115**, 021102 (2019).
 - ²⁴M. Pont, R. Albiero, S. E. Thomas, N. Spagnolo, F. Ceccarelli, G. Corrielli, A. Brioussel, N. Somaschi, H. Huet, A. Harouri, A. Lemaitre, I. Sagnes, N. Belabas, F. Sciarrino, R. Osellame, P. Senellart, and A. Crespi, “Quantifying n-photon indistinguishability with a cyclic integrated interferometer,” (2022), [arXiv:2201.13333 \[quant-ph\]](https://arxiv.org/abs/2201.13333).
 - ²⁵S. F. Covre da Silva, G. Undeutsch, B. Lehner, S. Manna, T. M. Krieger, M. Reindl, C. Schimpf, R. Trotta, and A. Rastelli, *Appl. Phys. Lett.* **119**, 120502 (2021).
 - ²⁶L. Schweickert, K. D. Jöns, K. D. Zeuner, S. F. C. D. Silva, H. Huang, T. Lettner, M. Reindl, J. Zichi, R. Trotta, A. Rastelli, and V. Zwiller, *Appl. Phys. Lett.* **112**, 093106 (2018).
 - ²⁷Y. H. Huo, A. Rastelli, and O. G. Schmidt, *Appl. Phys. Lett.* **102**, 152105 (2013).
 - ²⁸D. Huber, M. Reindl, S. F. C. da Silva, C. Schimpf, J. Martín-Sánchez, H. Huang, G. Piredda, J. Edlinger, A. Rastelli, and R. Trotta, *Phys. Rev. Lett.* **121**, 033902 (2018).
 - ²⁹M. Reindl, J. H. Weber, D. Huber, C. Schimpf, S. F. C. D. Silva, S. L. Portalupi, R. Trotta, P. Michler, and A. Rastelli, *Phys. Rev. B* **100**, 155420 (2019).
 - ³⁰E. Schöll, L. Hanschke, L. Schweickert, K. D. Zeuner, M. Reindl, S. F. C. da Silva, T. Lettner, R. Trotta, J. J. Finley, K. Müller, A. Rastelli, V. Zwiller, and K. D. Jöns, *Nano Lett.* **19**, 2404 (2019).
 - ³¹A. V. Kuhlmann, J. Houel, D. Brunner, A. Ludwig, D. Reuter, A. D. Wieck, and R. J. Warburton, *Rev. Sci. Instrum.* **84**, 073905 (2013).
 - ³²A. L. Efron and M. Rosen, *Phys. Rev. Lett.* **78**, 1110 (1997).
 - ³³H. Ollivier, S. E. Thomas, S. C. Wein, I. M. De Buy Wenniger, N. Coste, J. C. Loredó, N. Somaschi, A. Harouri, A. Lemaitre, I. Sagnes, L. Lanco, C. Simon, C. Anton, O. Krebs, and P. Senellart, *Phys. Rev. Lett.* **126**, 63602 (2021).
 - ³⁴A. Thoma, P. Schnauber, M. Gschrey, M. Seifried, J. Wolters, J. H. Schulze, A. Strittmatter, S. Rodt, A. Carmele, A. Knorr, T. Heindel, and S. Reitzenstein, *Phys. Rev. Lett.* **116**, 033601 (2016).
 - ³⁵D. Huber, M. Reindl, Y. Huo, H. Huang, J. S. Wildmann, O. G. Schmidt, A. Rastelli, and R. Trotta, *Nat. Commun.* **8**, 15506 (2017).
 - ³⁶C. Schimpf, M. Reindl, P. Klenovský, T. Fromherz, S. F. Covre Da Silva, J. Hofer, C. Schneider, S. Höfling, R. Trotta, and A. Rastelli, *Opt. Express* **27**, 35290 (2019).
 - ³⁷N. Somaschi, V. Giesz, L. De Santis, J. C. Loredó, M. P. Almeida, G. Hornecker, S. L. Portalupi, T. Grange, C. Antón, J. Demory, C. Gómez, I. Sagnes, N. D. Lanzillotti-Kimura, A. Lemaitre, A. Auffeves, A. G. White, L. Lanco, and P. Senellart, *Nat. Photonics* **10**, 340 (2016).
 - ³⁸N. Tomm, A. Javadi, N. O. Antoniadis, D. Najer, M. C. Löbl, A. R. Korsch, R. Schott, S. R. Valentin, A. D. Wieck, A. Ludwig, and R. J. Warburton, *Nat. Nanotechnol.* **16**, 399 (2021).
 - ³⁹E. A. Muljarov and R. Zimmermann, *Phys. Rev. Lett.* **93**, 237401 (2004).
 - ⁴⁰H. Wang, Z.-C. Duan, Y.-H. Li, S. Chen, J.-P. Li, Y.-M. Y. He, M.-C. Chen, Y.-M. Y. He, X. Ding, C.-Z. Peng, C. Schneider, M. Kamp, S. Höfling, C.-Y. Lu, and J.-W. Pan, *Phys. Rev. Lett.* **116**, 213601 (2016).
 - ⁴¹T. Hummel, *Multiphoton generation from a single quantum dot in a photonic nanostructure*, Ph.D. thesis, University of Copenhagen (2019).
 - ⁴²X. Ding, Y. He, Z.-C. C. Duan, N. Gregersen, M.-C. C. Chen, S. Unsleber, S. Maier, C. Schneider, M. Kamp, S. Höfling, C.-Y. Y. Lu, and J.-W. W. Pan, *Phys. Rev. Lett.* **116**, 020401 (2016).
 - ⁴³J. Liu, R. Su, Y. Wei, B. Yao, S. F. C. da Silva, Y. Yu, J. Iles-Smith, K. Srinivasan, A. Rastelli, J. Li, and X. Wang, *Nat. Nanotechnol.* **14**, 586 (2019).
 - ⁴⁴A factor of two faster EOMs should be feasible according to the manufacturer.